
Article:
Nassar, M., Bogomolov, K., Grishina, E. et al. (2 more authors) (2025) Towards eco-friendly batteries: high temperature baking of carbonaceous (MCMB) Li-ion anodes containing advanced water-based natural polymer binders results in superior performance. Journal of Solid State Electrochemistry. ISSN: 1432-8488

https://doi.org/10.1007/s10008-025-06402-1

Journal of Solid State Electrochemistry
https://doi.org/10.1007/s10008-025-06402-1

ORIGINAL PAPER

Towards eco-friendly batteries: high temperature baking of carbonaceous (MCMB) Li-ion anodes containing advanced water-based natural polymer binders results in superior performance

Maisam Nassar[1] · Katerina Bogomolov[1] · Ekaterina Grishina[1] · Yair Ein-Eli[1,2,3] · Nadav Amdursky[2,4,5]

Received: 3 July 2025 / Revised: 27 July 2025 / Accepted: 30 July 2025

Abstract
Replacing common polymeric binder materials in lithium-ion batteries (LIBs) with more sustainable and environmentally friendly options is one of the challenges in designing new generations of LIBs. Here, we explain how incorporating protein-based polymers into the binder formulation can enhance binder performance in the graphite anode of LIBs. The electrode preparation with these binders involves an atypical thermal treatment ("baking") that causes structural transformation. The effect of baking temperature on battery performance is examined using various methods covering morphological, structural, and electrochemical aspects. We find that baking the binders at temperatures above 120 °C removes tightly bound water molecules, which impair LIB performance. Water removal promotes intra- and inter-molecular bond formation among the binder components, while the primary covalent structure of these binders remains unchanged. Ultimately, using thermally treated binders enhances the electrochemical performance of graphite anodes and provides strong adhesion. The ideas presented here could significantly influence the design of new binders for LIBs.

Keywords Li-ion batteries · Graphite · Anode · Protein-based binder · High-temperature baking

Introduction

Lithium-ion battery (LIB) technology is extensively used in modern technological applications, including various electronic devices and electric vehicles [1]. Several essential components are needed to produce LIBs, and each one is vital to the electrochemical battery's functioning. One of these key components is the anode, which is a composite electrode consisting of a copper foil current collector coated with an active material that is mixed with a conductive material and bonded with a polymeric binder.

The binder's primary role is to maintain particle cohesion and ensure adhesion between the electrode film and the current collector. This is crucial in order to support an electronic network with a certain level of electrode uniformity to facilitate the electrochemical reaction [2]. At the same time, binders are often considered electrochemically inactive materials and often insulating materials whose percentage should be kept as low as possible. Therefore, understanding the properties of a binder in the composite electrode is essential, allowing improvement of the battery performance.

Various binders have been evaluated with mesocarbon microbeads (MCMB) graphite anodes. The most common one used in commercial LIBs is polyvinylidene fluoride (PVDF) (Scheme 1) for both negative and positive electrodes, mainly due to its good cycling electrochemical stability [3]. However, PVDF binder application obligates using a toxic and highly volatile organic solvent, N-methyl-2-pyrrolidone (NMP) [4]. Production costs during electrode manufacturing based on NMP as a carrying medium are highly energetically consuming, at least one order of magnitude

✉ Yair Ein-Eli
eineli@technion.ac.il

1 Department of Materials Science and Engineering, Technion – Israel Institute of Technology, Haifa 3200003, Israel

2 Grand Technion Energy Program (GTEP), Technion – Israel Institute of Technology, Haifa 3200003, Israel

3 Israel National Institute for Energy Storage (INIES), Technion – Israel Institute of Technology, Haifa 3200003, Israel

4 Chemistry, School of Mathematical and Physical Sciences, University of Sheffield, Western Bank, Sheffield, S10 2TN, UK

5 Schulich Faculty of Chemistry, Technion – Israel Institute of Technology, Haifa, 3200003, Israel

Published online: 14 August 2025

Scheme 1 Chemical structures of PVDF, CMC, SBR, and BSA

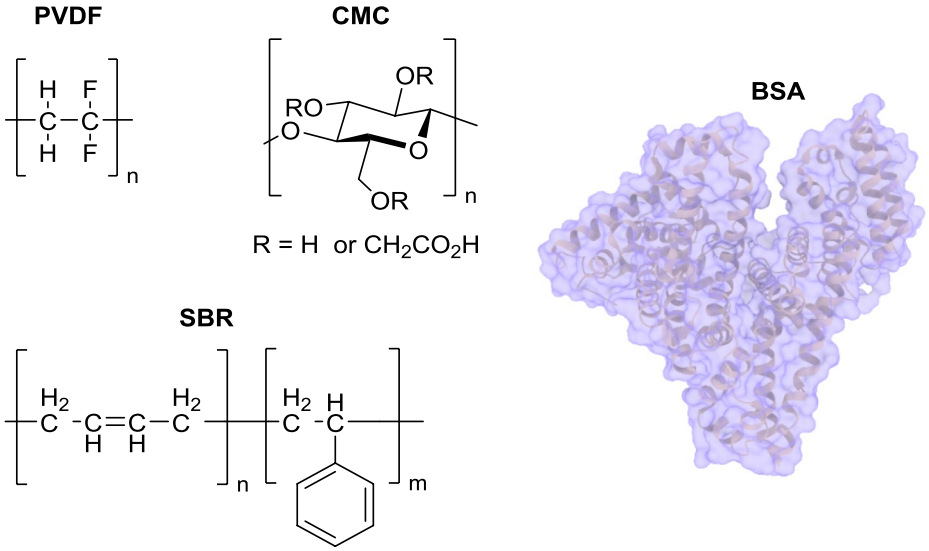

higher when compared to water-based electrodes [5]. Moreover, PVDF binder is relatively expensive to acquire. An additional advantage of fabricating electrodes with water-based binders is the simplicity of the recycling procedures, which allow for substantially higher recovery of the electrode's active materials.

On the other side, water-processed electrodes pose potential challenges, including exposing the lithium-ion reservoir in the electrolyte to residual water. It can lead to undesirable side reactions, resulting in electrolyte degradation, lithium-ion depletion, and a poor solid electrolyte interphase (SEI) [6] layer that cannot adequately protect the graphite surface [6]. The $LiPF_6$ salt, which is traditionally dissolved in the organic electrolyte (composed of ethylene carbonate: dimethyl carbonate (EC:DMC)), is known for its high reactivity with water traces, forming hydrofluoric (HF) acid and gaseous POF_3. HF contributes protons for further reacting with PF_6^- ions, generating PF_5 [7]. Both POF_3 and PF_5 react further with water to form more HF (and other acidic species of the form HPO_xF_y). This process is the primary source for lithium-ion depletion, drastically decreasing their availability [8]. The aforementioned products lead to an additional degradation path that reduces the electrolyte content. As PF_5 is a strong Lewis acid, which is also associated with the catalysis of cyclic carbonate ring opening, it leads to the degradation of common electrolytes based on ethylene carbonate [8, 9]. HF formation can additionally provoke another degradation path, which includes destabilization of the formed SEI, leading to repeated SEI formation and continuous reversible capacity loss. The gradual exchange of the SEI composition may impose a higher energy barrier for lithium-ion diffusion to the graphite [10]. Furthermore, at elevated water concentrations, water molecules are likely to compete with other electrolyte components and react directly at the electrode surface, forming passivating products. The resulting surface films are composed of LiOH and Li_2O, along with products from salt and solvent decomposition [11, 12]. These products are known for their negative impact on lithium-ion mobility and rather low ability to protect from further electrolyte deterioration. Since water contamination may hold such a significant effect on the electrochemical performance and stability in the organic medium, the effect of baking temperature on water-bearing binders must be tested.

Here, we compare a known formulation of a binder, sodium carboxymethyl cellulose (CMC) in combination with styrene butadiene rubber co-polymer (SBR) [13–15], to a novel binder composition made by a cross-linked protein biopolymer composed of the bovine serum albumin (BSA) protein (Scheme 1 for all chemical structures). Both water-based binders differ in their chemical composition. BSA is a protein-based binder that contains various functional groups, including carboxylic acid (–COOH), hydroxyl (–OH), and amino ($–NH_2$) groups. The strategy behind the polymerization process involves utilizing the cysteine amino acid residues in BSA to enable crosslinking between different protein molecules via S–S bonds, thereby forming a cross-linked protein network [16]. The CMC:SBR binder system has been widely studied for its effectiveness as a binder in Li-ion battery anodes [13–15]. It is a copolymer binder that integrates the distinct chemical properties of CMC and SBR. CMC contains various functional groups, such as carboxylic acid (–COOH) and hydroxyl (–OH), which contribute to its adhesion and dispersion capabilities [17]. In contrast, SBR primarily consists of non-polar carbon–hydrogen (C–H) bonds, providing mechanical flexibility and elasticity. The selection of this binder was aimed at comparing different water-based binder systems and gaining insight into the working mechanisms of such binders in Li-ion battery applications. In our new process, subsequent to slurry casting, the electrodes

were subjected to thermal treatment to vaporize the aqueous carrying medium at an untraditionally higher temperature of 200 °C compared to 120 °C. The drying process for the anodes at this atypical temperature is termed here as "baking." The changes and modifications in the chemical structure of the binders were studied, and the impact on the electrochemical performance of the graphite anode was assessed, showing a significant improvement in the performance of the protein-based biopolymer, hence opening a new horizon for a new generation of binder materials.

Experimental

Anode preparation

The active material used for the graphite anodes fabrication was a commercial graphite powder, MCMB (MTI Corporation), with a BET specific surface area of 2.022 m^2g^{-1}. Two different binders were used: (i) carboxymethyl cellulose (NaCMC, Sigma Aldrich) with styrene-butadiene rubber copolymer (SBR, Sigma Aldrich), mixed in deionized water and (ii) protein-based binder, cross-linked bovine serum albumin (BSA, MP Biomedicals), for which polymerization and crosslinking are discussed elsewhere. PVDF binder (MTI corporation) was used as a reference. Anode slurries were prepared with a 90:10% w/w of MCMB to binder ratio in different carrier media. First, as a reference, PVDF-based slurry was prepared by premixing 9% w/w PVDF in NMP. Then, 1.1 g of the binder solution was added to 0.9 g of MCMB and stirred overnight. Presumably, no external water was added to this slurry, and any trace that was found later by the TGA analysis originated from adsorbed moisture (up to 10% from the binder weight). Then, the first water-bearing slurry, the CMC:SBR-based slurry, was prepared in a three-stage process. In the first step, 0.4 g CMC was added to 20 ml of warm water at 40 °C for 2 h. Then, the solution was cooled to room temperature, and 0.6 g SBR was stirred into the solution and left to stir overnight. Lastly, 0.9 g of MCMB was mixed with 2.1 g of the binder solution overnight. Such high water content, of about 66% w/w from the slurry, is required for slurry casting. The second water-bearing binder, the BSA biopolymer, was prepared as described by Amdursky et al. [16], involving dissolving the BSA protein in TFE:water (4:1), followed by the addition of 2-mercaptoethanol and ethylenediamine. The role of the TFE:water mixture is to denature the protein for the effective reduction of the intramolecular disulfide bonds within the protein using the 2-mercaptoethanol reducing agent. The addition of ethylenediamine is to promote intermolecular disulfide bonds, hence the crosslinking of the biopolymer. It is worth mentioning that although cross-linked proteins generally exhibit solid or jell-like properties, the deliberate addition of water as a solvent was intended to maintain a workable viscosity suitable for slurry preparation and electrode coating. It is important to note that TFE is by no means an "eco" solvent, but currently, it is necessary for the denaturation step [18, 19]. Nevertheless, following crosslinking and binder formation, the TFE is evaporated and not present in the final binder formulation, unlike any other polymers that are per- or polyfluoroalkyl substances (PFAS), such as PVDF. Moreover, as shown in the original work on the BSA-based polymer [16], the TFE can be easily recycled during the final binder-making process as it evaporates and is captured in situ owing to its low boiling point, requiring less energy [20–22] compared to NMP. Nonetheless, future use of the BSA-based binder should involve a transition to more water-based formulations or "greener" denaturing agents such as urea [23]. In terms of sustainability, BSA is recoverable and biodegradable, while PVDF is considered non-degradable.

The preparation process of the BSA-based slurry included direct mixing of the previously prepared mixture of BSA of concentration of 30 mg ml^{-1}, total of 3.92 ml of binder solution, with 0.9 g of MCMB, overnight at room temperature. About 20% w/w of the solvent in the binder solution is based on water, which means that the water content in the slurry is at most 16% w/w.

Flow curves were measured using a DVNext cone/plate Rheometer (Brookfield, Ametek) with a CPA-52Z spindle. The gap between the cone and the plate was set at 0.0005 in. The temperature was kept constant at 180 °C throughout the measurements. The volume of each sample was 0.5 ml. The curves were recorded at shear rates ranging from 0.02 to 100 s^{-1}. Equilibrium was reached in 60 s. As obtained from Correau model fitting of the data, seen in Fig. S1, the zero shear viscosity of the slurries are 65.73 ± 1.79 Pa s, 140.69 ± 14.59 Pa s, and 118.82 ± 19.87 Pa s for PVDF-, CMC:SBR-, and BSA-based slurries, respectively ($R^2 > 0.99$).

Finally, each slurry was cast onto a copper foil using a Dr. Blade coater (MTI Instruments). The thickness of the film was set to 20 µm for all the electrodes to maintain approximately similar loadings. The electrodes were baked at 120 °C and 200 °C under vacuum for 24 h and then punched into small discs with a diameter of 12.5 mm.

Electrochemical characterization

Electrochemical characterization of the anodes was performed in half-cell vs. Li metal in a Swagelok cell (or a T cell). The assembly of the cells was carried out in an argon-filled glove box. A three-electrode cell was based on MCMB anode as the working electrode, and Li as both the counter and reference electrodes. Two layers of microporous separator (Whatman® glass microfiber filters, 1.6 µm pore size

and 0.26 mm thick) were utilized. Finally, the cell was filled with 200 µL electrolyte solution of 1.0 M $LiPF_6$, EC:DMC, 1:1 v/v (Sigma-Aldrich). The electrode loading ranged from 4 to 6 mg cm^{-2}.

The cycling performance of the assembled T cells was studied using BT2000 battery test system (Arbin Instruments, USA). Galvanostatic charge–discharge (GCD) cycling was carried out applying a C-rate of C/12, between a voltage range of 0.01 and 2.5 V vs. Li^+/Li. Kinetics via cyclic voltammetry (CV) measurements and electrochemical impedance spectroscopy (EIS) measurements were acquired using VSP-3e potentiostat/galvanostat (BioLogic, France). The CV measurements were conducted in a potential range of 0.005–1.5 V vs. Li^+/Li at a scan rate of 0.01 mV s^{-1}. EIS testing was done in a frequency range of 100 kHz to 0.01 Hz with an AC voltage amplitude of 10 mV versus open circuit potential. The obtained Nyquist plots were modeled and fitted into an electric circuit described by the following equation, using EC-lab software:

$$R_s + Q_{SEI}/R_{SEI} + Q_{ct}/R_{ct} + W \quad (1)$$

where R is resistivity, Q is capacity, and W is Warburg diffusion element.

Physical characterization

The morphological structure of the studied anodes was analyzed using scanning electron microscopes (SEM): high-resolution SEM (Zeiss, Ultra plus) and a Phenom™ XL G2 Desktop SEM (Thermo Fischer Scientific). Additionally, to evaluate the structural change occurring due to the baking process, physisorption measurements were conducted using a TriFlex porosimeter (Micromeritics) in a nitrogen environment. Samples were pre-dried at 120 °C for 12 h in a vacuum, and BET analysis was done using MicroActive software. While the obtained isotherms for MCMB were not consistent with the BET model, other samples were scrabbed from anodes based on Super P Conductive Carbon Black (MTI) instead of MCMB with the various binders, since a larger BET surface, 62 m^2 g^{-1}, was required as a case study for the binder effect.

The thermal stability of the different binders was tested utilizing a TGA2 (Mettler Toledo) for thermal gravimetric analysis (TGA). Two samples were tested for each binder; samples were analyzed in air and nitrogen. The binder samples were dried and kept at 60 °C a night before and then heated at 10 °C min^{-1} up to 700 °C. Chemical changes during baking were assessed using Fourier transform infrared spectroscopy (FTIR) and RAMAN spectroscopy. FTIR analysis was conducted using Nicolet iS50 FTIR Spectrometer (Thermo Fisher). Absorbance intensity of each baked pristine binder was measured using attenuated total reflectance (ATR) mode. Powder samples, like MCMB and scrabbed anodes, were tested using potassium bromide (KBr) pellets (Specac Ltd) by transmission detector mode. The samples were prepared using 250 mg of KBr and approximately 2 mg of dry slurry. The mixture was dried in a 60 °C oven before being pressed. The experimental setup was default, with 32 scans and a resolution of 4 cm^{-1}. Raman spectroscopy was obtained using WITec Alpha300 Raman imaging microscope (Oxford Instruments), with laser wavelength of 532 nm and a CCD detector. The measurement setup consisted of a grating of 300 g mm^{-2}, laser power of 10 mW, acquisition time of 3 min, and an integration time of 0.5 ms.

Lastly, the adhesion was rated using adhesive tape. Samples were cut off the greater electrode in a selected area free of any visible imperfections. Two cuts were made using a stainless-steel scalpel along the diagonal of each sample, forming an *x* cut in the middle. Double-coated polyethylene foam tape (3 M), with peel adhesion greater than 10 N cm^{-1}, was placed on top of each intersection and smoothed by light pressing with a glass slide to ensure there is no air trapped beneath. Within 1 min, the tape was pulled off rapidly back upon itself, and the *x* cut area was inspected.

Results and discussion

Physical characterization of the binders

Thermal stability of the binders

The thermal stability of the binders and their water retention were investigated using TGA analysis. The graphs for CMC:SBR and BSA binders are shown in Fig. 1a, b, respectively. The TGA data indicate that the initial weight drop for BSA and CMC:SBR binders occurred between 205 and 227 °C and originated primarily due to water loss. In the case of CMC:SBR, the first degradation step that was associated with binder decomposition was observed around 245 °C, a drop from ~ 83 to 50 wt%. The significant weight loss seen in the first phase (33%), between 245 and 320 °C, is associated with the loss of the structural integrity of the main polymeric binder, i.e., CMC. Next, the degradation step of the binder chemical bonds took place between 320 and 450 °C; at this stage, the weight drop was approximately 15%. This step is associated with the structural degradation of the second binder, i.e., SBR. The last step of weight loss of about 5 wt%, between 450 and 600 °C, appeared in the TGA curve in an air environment but not in the one in a N_2 gas environment; hence, the final degradation step is probably ascribed to the burning reaction for the CMC:SBR binder.

The water release process for the BSA binder was completed at approximately 227 °C in both air and N_2 conditions,

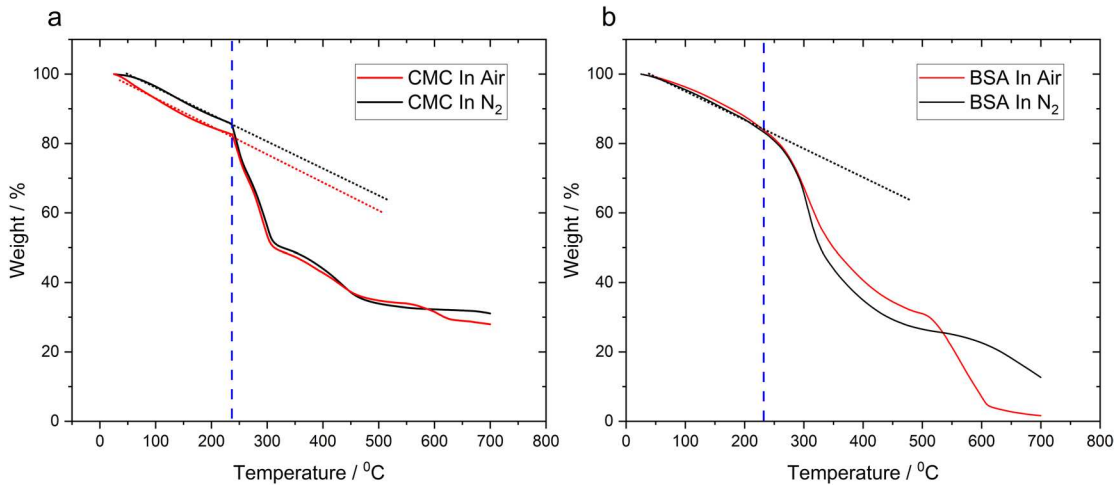

Fig. 1 TGA graph of (**a**) CMC:SBR and (**b**) BSA binders in air and in N_2 environments

exhibiting a resemblance to the CMC:SBR. According to the curves presented in Fig. 1b, the degradation process consisted of two stages: the first stage occurred in the temperature range of 250 to 500 °C, resulting in a 49% weight loss, and the second stage involved the burning reaction of the BSA binder, which is not present in an oxygen-free environment, i.e., N_2.

Based on these findings, it is reasonable to conclude that the binders remain stable within the whole temperature range used for electrode preparation and baking, i.e., ranging from room temperature to the extremity of 200 °C. Nonetheless, for both types of binders, water release continues slightly beyond 200 °C, and total deterioration occurs at temperatures well above. Just for comparison, the standard temperature range for the PVDF-graphite-based anode preparation process is typically 80–120 °C. Therefore, 120 and 200 °C were chosen as the baking temperatures for the anodes in order to assess the impact of the residual entrapped water compared to almost complete moisture removal, correspondingly.

To compare the thermal stability of PVDF, we performed TGA analysis on this binder as well. As can be seen in Fig. S2, the PVDF binder contained approximately 10% water, probably from water adsorption during storage. Since the carrying medium for PVDF is NMP and not a water-based solvent, this amount is considerably lower compared to the other two binders. Also, the key distinction in water release between the PVDF binder and the BSA and CMC binders lies in the release rate, with PVDF exhibiting its highest release rate between 60 and 100 °C.

Understanding the chemical modification during the baking process via FTIR and Raman spectroscopy

One of the primary goals of this study is to determine the effect of elevated temperatures on water-soluble binders. Since water is known to negatively impact the performance of LIBs, it is required to evaporate all of the water molecules trapped inside the binder's polymeric chains, which motivates the anode baking procedure at high temperatures. As the process of evaporation may also involve chemical changes of the binders in the slurry at these temperatures, we used FTIR to assess any noticeable structural changes during the baking process.

First, spectra of pristine MCMB powder were taken as received directly from the original package and after baking to 200 °C. Figure 2a demonstrates typical peaks ascribed to MCMB, i.e., two peaks in the wavelength range of 2500–3000 cm^{-1}, a broad peak at 3300–3550 cm^{-1}, and a pair of peaks at 1600 and 1440 cm^{-1}. The former is assigned to C–H stretching of aromatic and aliphatic hydrogen and is present at both temperatures [16, 24–26]. The second could be assigned to O–H stretching vibration of adsorbed moisture or stretching vibration of phenolic OH groups [25, 27, 28]. This peak is seen only at room temperature, while the spectrum of baked powder at 200 °C lacks it. The absence of this peak after baking confirms the first suggestion, as does the significant loss of water indicated in the TGA data. Lastly, the peaks at 1600 and 1440 cm^{-1} are attributed to the aromatic nature of MCMB, e.g., C = C in-plane bending and scissoring [25]. Besides the previously described attributions, no additional peaks can be identified in the spectra, dismissing the presence of other functional groups on the carbonaceous active material.

The next step was to collect the spectra of the grated electrodes, made of MCMB combined with the different binders, i.e., BSA or CMC:SBR. The obtained spectra are displayed in Fig. 2. In both Fig. 2b, c, at least two distinct peaks can be observed in the wavelength region of 3000–3600 cm^{-1}, only observed upon the addition of MCMB. After baking at 120 °C, a broad unresolved peak is observed for both

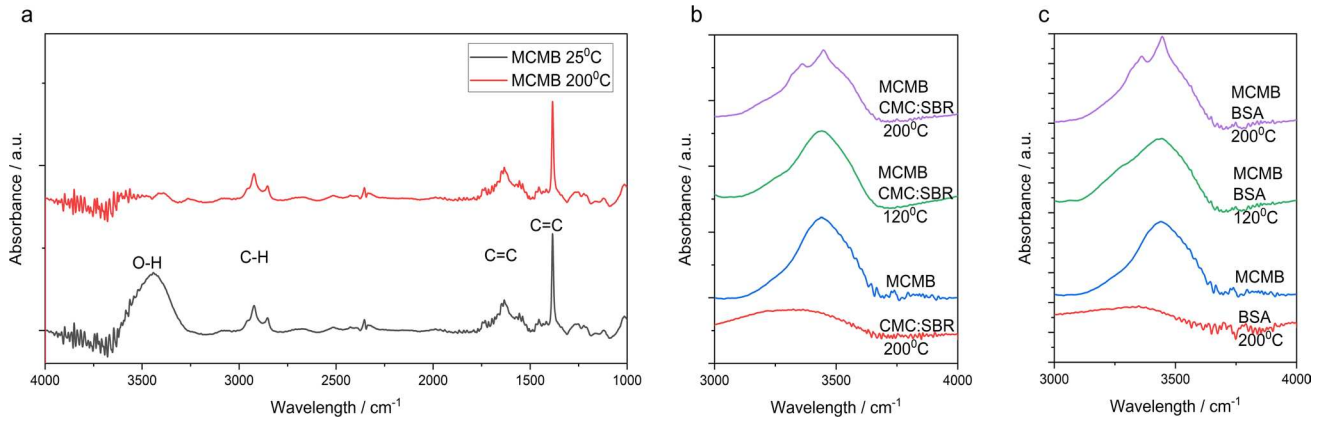

Fig. 2 Absorbance FTIR spectra for (**a**) pristine, as received, at room temperature MCMB powder and for MCMB powder baked at 200 °C in vacuum for 12 h, and for pristine MCMB, pristine binders and anode materials baked at 120 and 200 °C (3000 to 4000 cm^{-1} range); **b** CMC:SBR-based electrode; **c** BSA-based electrode

binders. As previously stated, these peaks are most likely a consequence of O–H stretching, with water molecules entrapped in the aqueous slurry carrying medium. This statement is corroborated by the TGA curves presented earlier. Nevertheless, the structure of both binders has many characteristic functional groups, as presented in Scheme 1. BSA is a polypeptide, based on an amide backbone with amine and carboxyl termini, with additional residual side-chain groups like carboxyls, amines, phenols, hydroxyls, and thiol. All these groups are dictating the spatial structure of the protein. CMC:SBR is also characterized by multiple functional groups, e.g., ethers, hydroxyls, and carboxylic acids. As many of the mentioned groups may contribute to the obtained convoluted broad peak in the shown range, it is difficult to resolve the exact interaction emerging from the baking temperature elevation. In addition, the spatial structural difference between both binders is suspected to affect the contact with MCMB, as will be confirmed in the next sections, especially when baking temperature is considered. BSA is a protein naturally having a specific secondary and tertiary structure in accordance with the solution conditions, e.g., temperature, pH, and solution ionic strength [29, 30]. However, even prior to baking, it could be speculated [28] that the adsorption dynamics of the protein include unfolding and spreading on hydrophobic graphitic entities [31]. This means that even prior to any of the elevated temperature applications, some form of denaturation is forced. This is why the discussion is not focusing on the change in the amide-related peaks [32] (full FTIR spectra can be found in Fig. S3). Additionally, herein, the BSA is crosslinked via disulfide bonds [16]; hence, prolonged exposure to elevated temperatures, well above the denaturation temperature [33], may induce further changes in the spatial arrangement, especially when prior adsorption is considered [34], and even induce irreversible degradation [35]. Therefore, the conformation of the protein is determined by MCMB particles, crosslinking, and baking at an extreme temperature, culminating in aggregation and the formation of localized intramolecular interactions [36] in the increasing absence of water through evaporation, which may be the reason for the peak narrowing [37].

As for the CMC:SBR binder, CMC is forming the network while SBR forms cohesion between the active material particles, enhancing the dispersion and reducing the aggregation [13, 38]. CMC fulfills its role as a network former by formation of intra- and inter-molecular bonds to stabilize the glycosidic linkage in the backbone and to enable parallel chain alignment, respectively [39, 40]. These bonds cause strong entrapment of water that induces undesired side reactions [41]. As seen by the TGA, water is still present in this scenario, resulting in a shrunk film that entraps residual water and has a similar effect of peak narrowing.

The final aspect that should be taken into account is the potential irreversible effect of such high baking temperature, e.g., thermal crosslinking of CMC [42] or degradation [35]. Crosslinking between hydroxyl and carboxyl groups or esterification is not seen in the full FTIR spectrum and, thus, cannot be ruled out. The decomposition process of CMC:SBR starts at temperatures above 200 °C. However, since anode baking was conducted under vacuum, a decrease in the decomposition temperature is likely to occur. The FTIR spectra collected for anodes baked at 200 °C support this assumption, exhibiting a decrease in the intensity of the carboxylic peak upon heating (1600 cm^{-1}). The last statement can also be applied to BSA, commonly possessing these functional groups.

To confirm the possible degradation of the binders, Raman spectra analysis of MCMB powder and anodes was acquired (Fig. 3). Figure 3a demonstrates that the CMC:SBR binder showed no formation of new peaks, indicating that

no degradation has occurred regardless of the chosen baking temperature; thus, the peaks observed in the FTIR spectra are most likely to be ascribed to residual water. The peaks marked by asterisks in the Raman spectra for CMC are ascribed to SBR (1005- and 3060- cm^{-1}) and CMC (2930 cm^{-1}) [43]. SBR is observed only in the spectrum of the baking temperature of 200 °C. This phenomenon can be supported by previous works [43, 44]. According to Hagiawara et al. [43], capillary effects drive the migration of SBR at elevated temperature, an observation that is not detected at room temperature. Concordantly, Kumberg et al. [44] state that fast drying rates impose inhomogeneous binder distribution due to binder migration. In contrast, comparing the BSA-based anode baked at 120 °C to the one baked at 200 °C (Fig. 3b) illustrates that increasing the temperature results in a change in the protein structure, ascribed to typical amide vibrational peaks (as shown by arrows: amide III; or secondary random coil conformation, at 1300 cm^{-1}, amide I; or random β-space, at 1676 cm^{-1}, and sidechain; methyl/methylene vibrations, at 2880–2940 cm^{-1}) [37]. It demonstrates that both temperature and the presence of MCMB result in a significant impact on protein conformations.

Binder-particle interface characterization via SEM

The anodes containing the binders of interest were imaged by SEM in order to characterize their surface morphology and the distinct interface contact between the binders and the MCMB particles in each of the studied baking temperatures. First, pristine MCMB powder was characterized with no binder addition to demonstrate the typical spherical shape of the particle and to ensure that the powder is of high purity using energy dispersive spectroscopy (EDS) (Fig. S4).

Next, electrodes based on MCMB with the binder were characterized via top-view high-resolution micrograph examination (Fig. 4), showing the distinct covering patterns of the binders. As shown in Fig. 4a, b, BSA binds to the MCMB particles and covers the anode surface, leaving only small parts of the anode particles uncovered. The network-to-surface contact formed by the cross-linked polymer BSA [42] enables homogeneous coverage of the electrode surface. This phenomenon is related to the desirable mechanical properties of the BSA-based polymer, which can stretch to five times its length [16]. Baking the anode at 200 °C triggers the decomposition of BSA, and the dense covering layer breaks down and shrinks, exposing more of the MCMB, as illustrated in Fig. 4b.

In contrast to BSA, the bonding mechanism of CMC:SBR is different and occurs locally at the edges of the spheres, rather than covering the entire surface, as demonstrated in Fig. 4c, d. This behavior can be explained by the SBR binder binding mechanism, which binds the particles by dot-to-surface contact, while CMC is characterized by segment-to-surface contact [41]. Upon baking these anodes to 200 °C, no meaningful change is observed, as seen in Fig. 4d compared to Fig. 4c. Traditionally used binder, i.e., PVDF, holds the same characteristic segment-to-surface binding behavior as CMC binder, and particle coverage resembles the one formed by BSA (Fig. S5).

The difference in the bonding mechanisms of BSA and CMC:SBR binders explains the variation in the surface area of the different anodes. While BSA interacts across the entire surface of the MCMB spheres, CMC:SBR interacts only at the edges. To further explore the different interaction modes between BSA or CMC:SBR and MCMB, we turned to BET analysis (Fig. 5). As seen in the calculated BET surface area (as calculated according to the obtained isotherms in

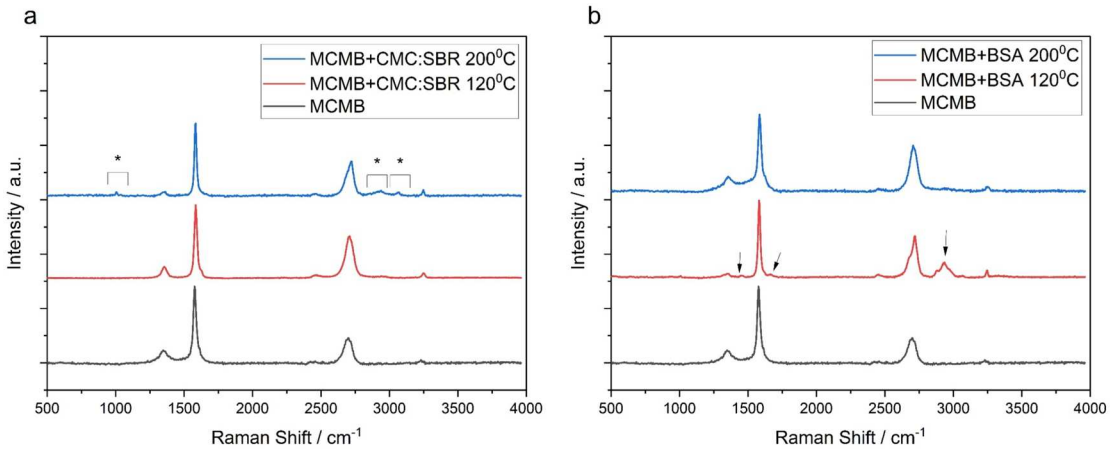

Fig. 3 Raman shift spectra of pristine MCMB and (**a**) CMC:SBR anodes baked at 120 and 200 °C; **b** BSA-based anodes baked at 120 and 200 °C

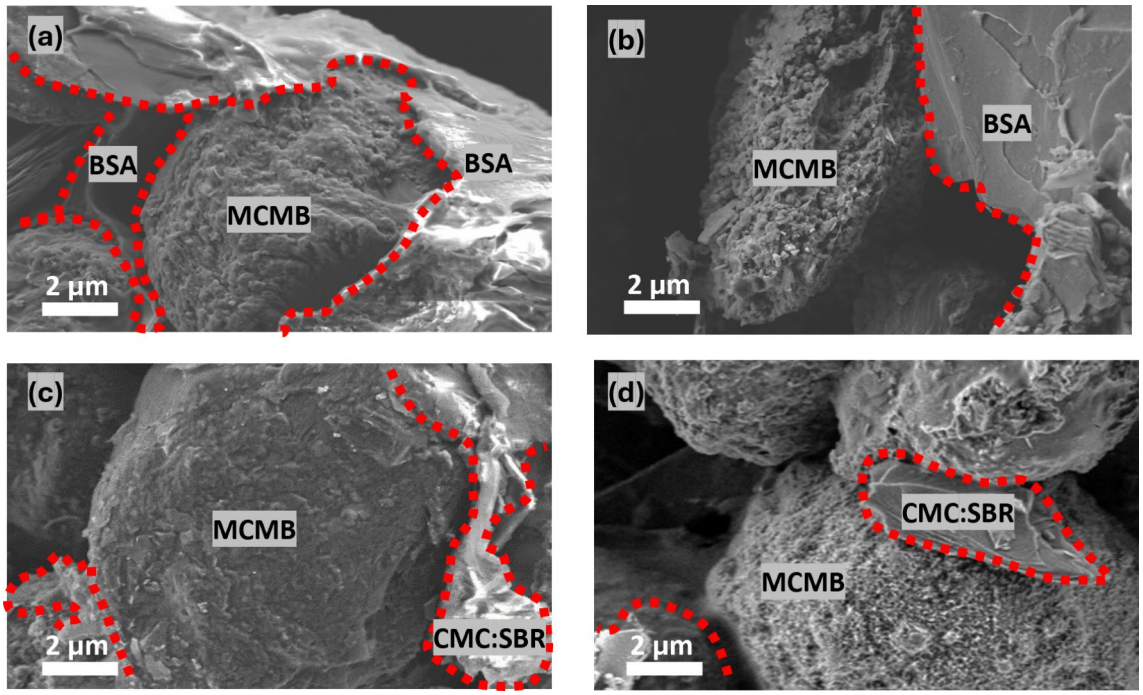

Fig. 4 HR-SEM micrographs of MCMB anodes, comparing the interfaces formed between the MCMB particles and (**a**) BSA at 120 °C; **b** BSA at 200 °C; **c** CMC:SBR at 120 °C; **d** CMC:SBR at 200 °C

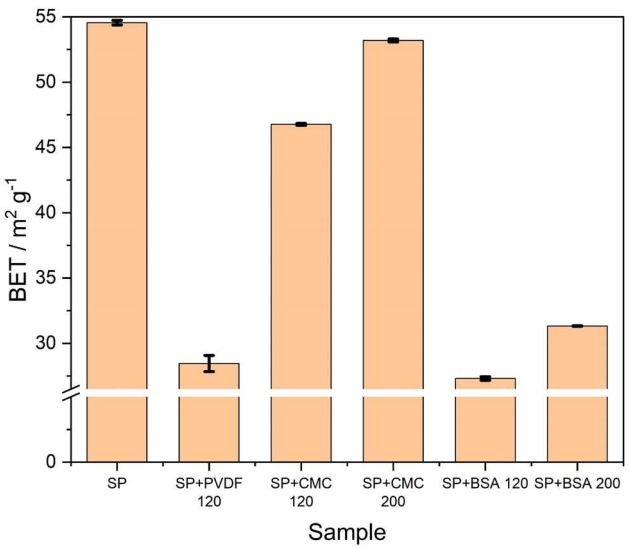

Fig. 5 BET surface area for pristine Super P carbon black (SP) and processed powder with PVDF, CMC, and BSA binders, baked at 120 and 200 °C

Fig. S6), CMC:SBR anodes exhibit a significantly higher surface area compared to BSA anodes.

SEM micrographs were further taken from the top view at a lower magnification (Fig. S7) to demonstrate the effect of baking temperature as a function of binder identity on the micro-porosity. As seen in the micrographs, voids formed between the MCMB particles following the baking process (circled in yellow), regardless of the binder identity. These voids originate from water evaporation during the baking process. Nonetheless, void formation in anodes based on CMC:SBR was more dominant than those based on BSA. It may indicate a higher content of free water present in this binder compared to BSA. However, the temperature increase does not seem to have a major impact on the concentration of voids in anodes containing CMC:SBR mixture. In contrast, the amount of voids in BSA-based anodes was higher when baked at 200 °C rather than at 120 °C. A possible suggested explanation is stronger bonding of water molecules to the BSA than to the CMC:SBR polymer mixture, which is more difficult to break, even upon heating to such high temperatures. These results are in agreement with the previously presented TGA results. The increase in the concentration of voids in the anodes may imply that the electrode tortuosity is lower, which in turn may facilitate the intercalation and deintercalation of lithium ions during electrode cycling.

To demonstrate the macro effect of the particle-to-binder interface seen in the SEM micrographs, a peeling test was performed (Fig. S8). As demonstrated and supported by the micrographs seen in Fig. 4, BSA and PVDF show approximately the same relative behavior where chunks are ripped off from the copper current collector, while CMC:SBR shows stronger relative adhesivity to the substrate and relatively lower cohesivity as mostly particles from the surface were ripped by the tape, emphasizing

the different contact type. In terms of the traditional peeling test, the jagged *x* cut for the PVDF-based anodes baked at 200 °C corresponds to the worst adhesion of the PVDF-based slurry to the current collector among the tested electrodes. In general, the adhesion seemed to weaken with the elevation of the baking temperature.

Electrochemical performance of the graphite anode in half-cell

In this section, we investigate how the binder identity and baking temperature affect the performance of composite anode electrodes in an electrochemical experimental setup. The key performance parameters tested were the capacity retention through galvanostatic cycling, overall kinetics via cyclic voltammetry, and electrochemical impedance spectroscopy.

Half-cells GCD cycling and Li-ion kinetics in the different MCMB anodes

Figure 6 shows the galvanostatic charge–discharge curves of MCMB anodes in half-cell configuration at C/12 rate. The different anodes presented in this set of results are prepared using either BSA or CMC:SBR binders and subsequently dried or baked at 120 °C and 200 °C. To illustrate the change in the capacity over cycling, only specific consecutive cycles are shown, i.e., cycles 1, 2, 5, 15, and 30.

In general, we observed a lower capacity for the anodes cycled after baking at 120 °C (Fig. 6a, c) compared to the anodes cycled after baking at 200 °C (Fig. 6b, d). This result can be attributed to the increased porosity at elevated temperatures, which in turn increases the surface area, thereby enabling lithium ion transport to the active material more efficiently. Moreover, loss of water traces may lead to less active material loss, and thus, the utilization is generally higher.

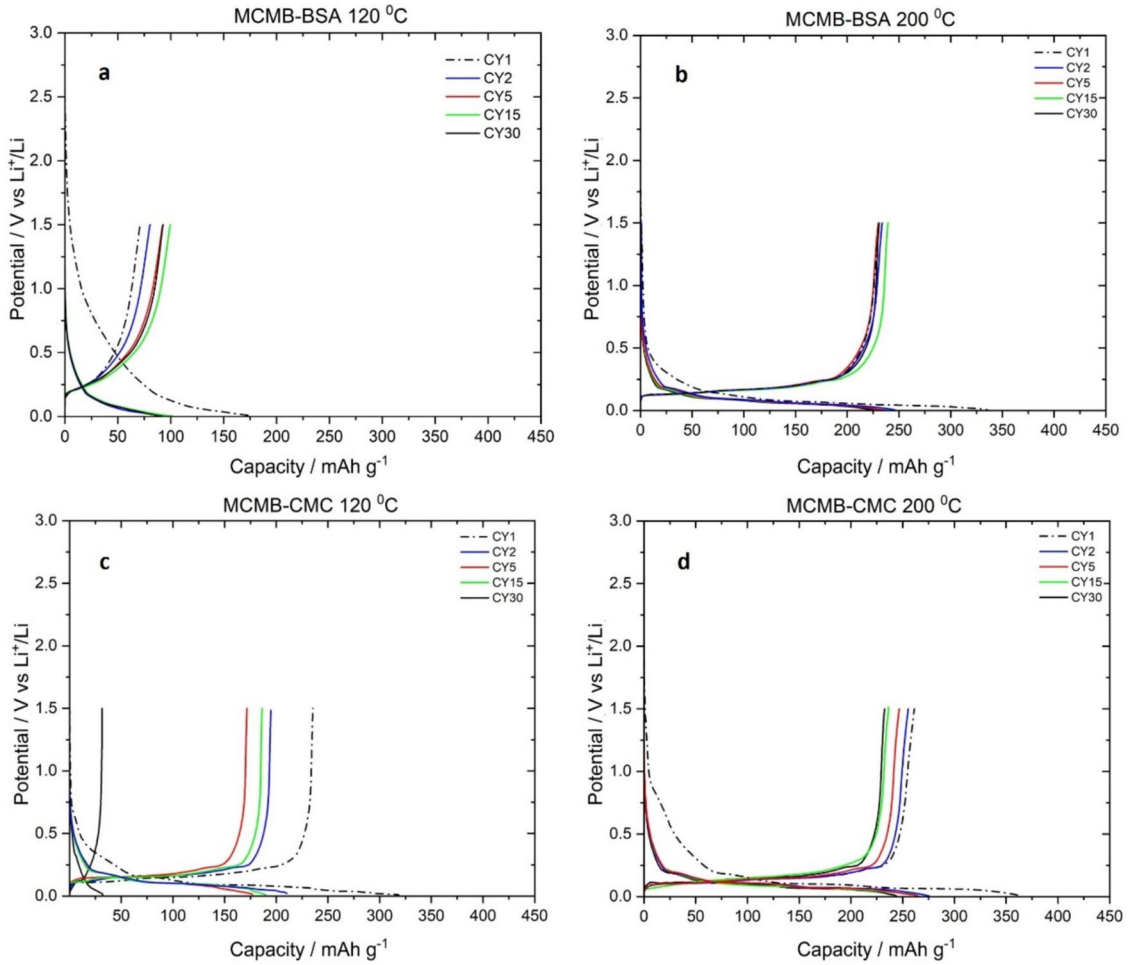

Fig. 6 Capacity-potential profiles of MCMB anodes upon repeated galvanostatic discharge–charge processes (vs. Li metal): **a**, **b** BSA binder and **c**, **d** CMC:SBR binder at drying temperature of **a**, **c** 120 °C and **b**, **d** 200 °C

The measurements reveal a substantial change in the electrochemical performance of the MCMB-BSA anodes as a function of temperature. The first discharge of the MCMB-BSA 200 °C anode reaches up to a capacity of 325 $mAhg^{-1}$, where the subsequent cycle fades to 240 $mAhg^{-1}$ (Fig. 6b). Nonetheless, the following cycles show almost no irreversible capacity (Fig. 7a). MCMB-BSA-based anodes baked at 120 °C (Fig. 6a) show substantially lower discharge capacity in the first cycle, i.e., 100 $mAhg^{-1}$, with pronounced overpotential around 1.8 V, probably originating from side reactions with water traces, unlike the common attribution of the overpotential to the SEI formation process. Importantly, the MCMB-BSA anodes are more stable and show high capacity retention over cycling when compared to the MCMB-CMC:SBR anodes (Fig. 6c, d), which gradually exhibit capacity loss as a function of cycling. Lower baking temperature in the case of BSA may result in the accumulation of higher residual water content, considering its small weight loss gradient and the protein structure that includes multiple hydrophilic groups.

Compared to the novel crosslinked BSA binder, the more common combination of the MCMB-CMC:SBR-based anodes, baked at 200 °C, shows discharge capacity of 365 $mAhg^{-1}$ at the first cycle, while the following discharge and charge capacities remain in the range of 200–220 $mAhg^{-1}$. MCMB-CMC:SBR-based anodes that were baked at 120 °C experienced a rapid capacity loss from 365 $mAhg^{-1}$ at the first cycle to less than 50 $mAhg^{-1}$ after 30 cycles. Unlike for the BSA-based anodes, for which the change in capacity is less prominent when comparing the baking temperatures of 120 °C and 200 °C, for CMC:SBR-based anodes, the capacity decay over cycling is notable. This may be related to the affinity to water and the open pore network, enabling relatively more efficient water content loss.

The results raise questions about the segregation behavior of the different binders during the drying process. While CMC:SBR-based anodes were previously shown to be less homogeneous over the depth of the electrode [45], our results suggest that the BSA binder in the slurry mixture may lead to better distribution over the electrode surface.

Figure 7 summarizes the capacity retention behavior of the different anodes over cycling and the Coulombic efficiency of charging and discharging. Although the MCMB-CMC:SBR-based anode baked at 200 °C demonstrates the highest achieved capacity, it shows considerably high irreversible capacity (Fig. 7b). This irreversible capacity loss is probably related to the continuous formation of SEI. The obtained surface area via the BET model indicates that CMC:SBR-coated particles baked at 200 °C exhibit relatively high and comparable values with pristine powder. This could mean that the coverage by the binder in this case is only partial, which is also demonstrated and supported by the SEM results. This observation suggests that the active material particles are relatively exposed to the electrolyte and, presumably, are provided with better lithium-ion transport due to high porosity. This state could exacerbate the catalytic decomposition of electrolyte components to produce SEI and possibly parasitic reactions with water traces, passivating the surface, leading to a decrease in energy density [46].

Cycling of BSA-based anodes (Fig. 7a) showed almost no irreversible capacity loss. This performance attribute can be associated with the MCMB particle coverage mechanism, which reduces the specific surface area and porosity,

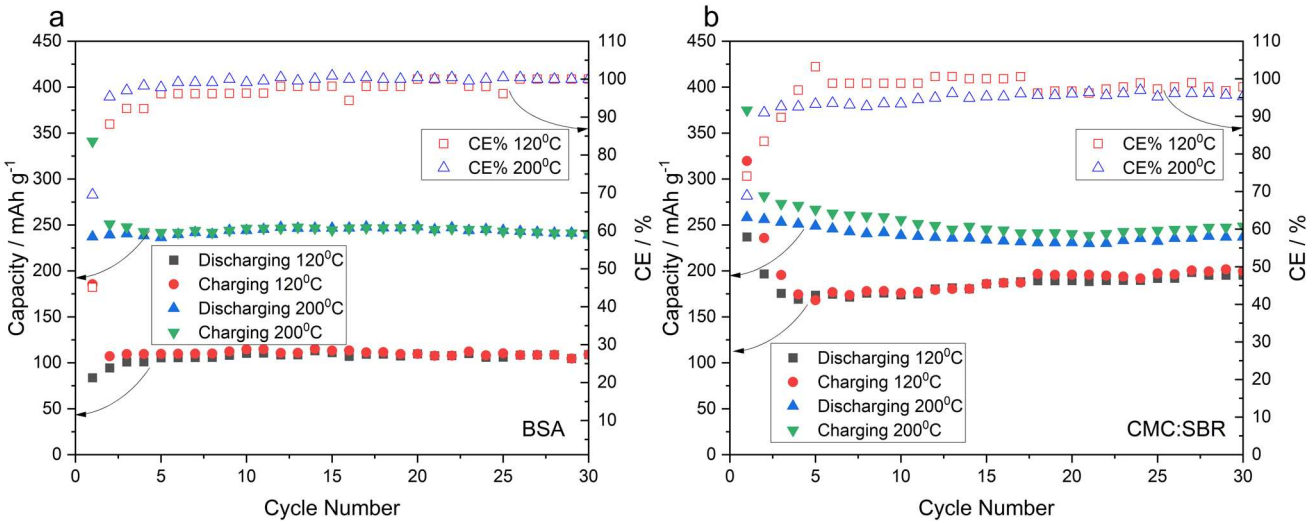

Fig. 7 Capacity measured upon galvanostatic charge–discharge cycling of MCMB anodes prepared with different binders: **a** BSA and (**b**) CMC:SBR. Baked at two baking temperatures of 120 and 200 °C; the anodes were cycled between 5 mV and 1.5 V at a rate C/12

resulting in controlled and short SEI formation and allowing for the avoidance of large irreversible capacity losses.

Hence, the increase in temperature, which seems to result in void formation, might provide a satisfactory explanation for the overall capacity increase when both BSA- and CMC:SBR-based anodes were baked at 200 °C, in addition to the elimination of parasitic reactions originating from residual water evaporation.

On this note, anodes based on slurries with the commonly used binder PVDF dissolved in NMP and baked up to 120 °C should be compared to the water-bearing slurries. As shown in Fig. S9a, the capacity of this anode shows relatively stable and comparable capacity with both CMC:SBR and BSA baked at 200 °C, i.e., 250 mAh g^{-1}. However, the CE is stabilized over a longer period, and the Coulombic efficiency is similar to that of CMC:SBR-based anodes and lower compared to BSA-based anodes baked at 200 °C. Performances of anode based on PVDF binder, baked at 200 °C (Fig. S9b) showed high instability in the Coulombic efficiency and major decrease in the recorded capacity.

In-depth studies of the first cycle of galvanostatic charge–discharge and cyclic voltammetry

Cyclic voltammetry (CV) was employed to explore further the effect of different binders, BSA or CMC:SBR, and the subsequent baking process temperatures, 120 °C and 200 °C, on the kinetics of the lithiation and de-lithiation process, and the SEI formation. The cells were first cathodically scanned from the open circuit potential (OCP, typically at a potential range of 2.8–3 V) to 0.005 V and then anodically to 1.5 V.

Figure 8 depicts the first galvanostatic charge–discharge cycle of MCMB-BSA-based anodes and the first scanned CV cycle. The galvanostatic charge–discharge cycle (Fig. 8a) clearly shows that baking at 200 °C results in higher capacity than at 120 °C. Baking at the lower temperature has exhibited an earlier reduction potential (starting at 1.8 V), which relates to irreversible lithium loss due to the consumption of lithium during the formation of the SEI and other earlier side reactions. The CV (Fig. 8b) depicts a broad peak generated for the BSA-based anode baked at 120 °C in a potential around 1.8 V, which does not appear in the high-temperature-baked electrode. It also indicates slower kinetics (lower current densities for Li-ion insertion and extraction), possibly due to the early occurrence of side reactions originating from Li-ion reactions with remaining water in the BSA binder. The parasitic reactions are shown to be probable and in accordance with the TGA results, as most of the entrapped water within the BSA binder was released during baking at 200 °C, unlike the one dried at 120 °C, which still contains water traces. SEI formation on the BSA-based anode baked at 200 °C occurs at a potential of 0.65 V, whereas the related SEI formation peak on the anode baked at 120 °C was shifted to a potential of ~ 0.5 V. The third reduction process (starts at 250–300 mV down to 0 V) corresponds to Li-ion intercalation. The subsequent anodic scan shows oxidation peaks appearing between 0.3 and 0.5 V, which corresponds to the de-lithiation process.

A similar evaluation was conducted for the CMC:SBR-based anodes (Fig. 9). In line with the results of the BSA-based binder, the galvanostatic charge–discharge curves show higher capacity recording, and the CV curves show higher lithiation and de-lithiation kinetics at higher baking temperatures. However, the magnitude of these changes is fundamentally different from the BSA-based binder electrode (Fig. 8). This observed difference can be discussed in light of the obtained porosity results. While pore size does not differ much, the overall pore volume differs greatly,

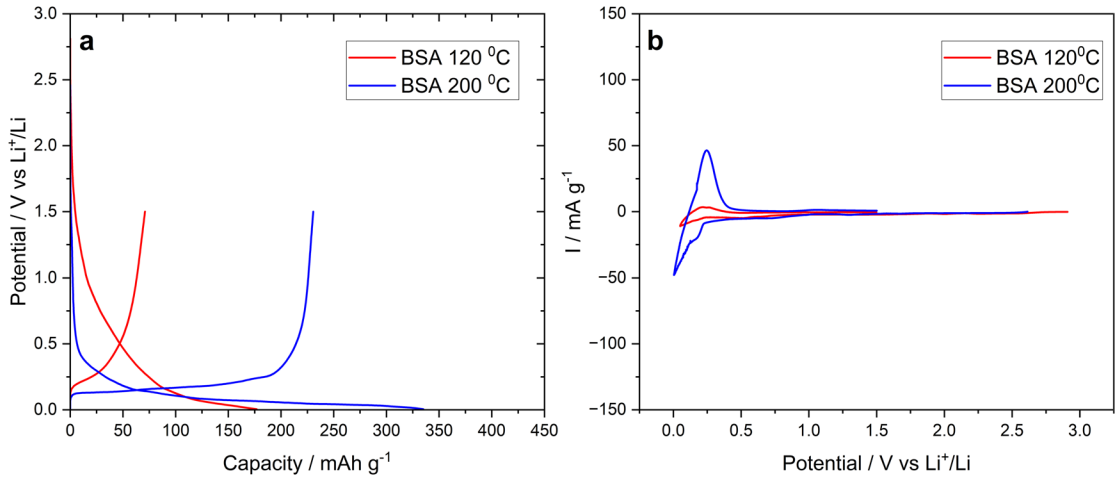

Fig. 8 First cyclic electrochemical behavior for MCMB-BSA anodes in baking temperatures of 120 °C and 200 °C: **a** First galvanostatically charge—discharge cycle of the anodes in both temperatures; **b** First cyclic voltammetry for the same anodes

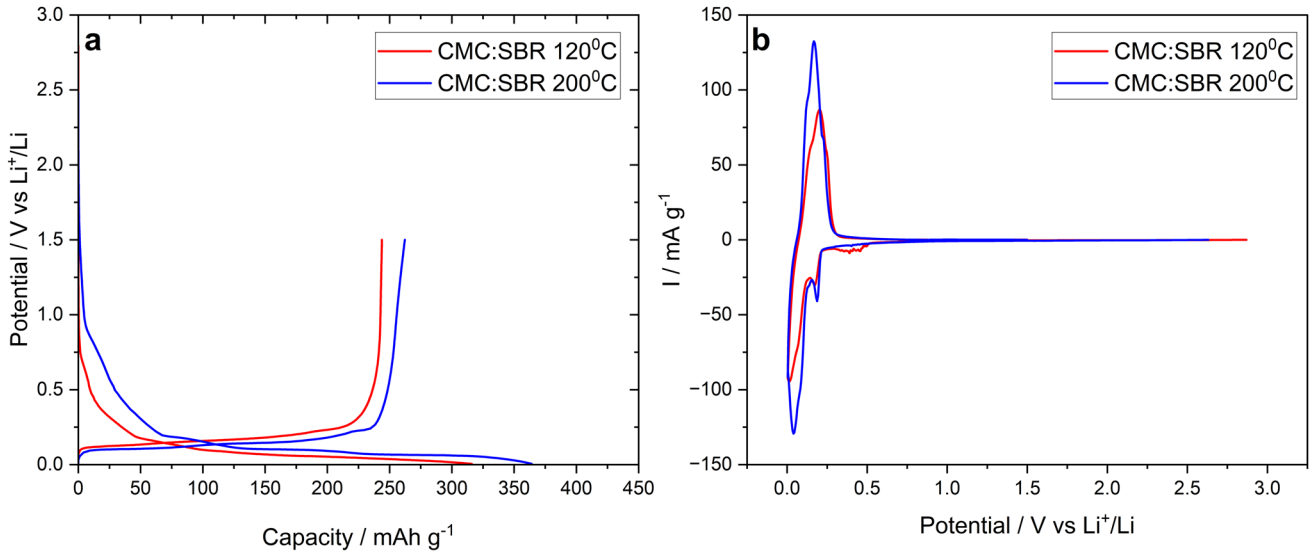

Fig. 9 First cyclic electrochemical behavior for MCMB-CMC:SBR anodes in baking temperatures of 120 and 200 °C. **a** First galvanostatically charge—discharge cycles of the anodes in both temperatures; **b** First cyclic voltammetry for the same anodes

resulting in effectively different surface areas, where higher pore volume is associated with larger surface area, providing more sites and pathways for lithium ions. Hence, the enlarged surface area results in enhanced capacity of CMC:SBR 200 °C compared to the analogous electrode baked at the lower temperature.

Furthermore, anodes made using CMC:SBR and baked at 200 °C show the formation of SEI at about 1.25 V, whereas for the anodes baked at 120 °C, the related SEI formation peak is shifted to 0.6 V. Regardless of the baking temperature, CMC:SBR-based anodes have substantial irreversible capacities, while anodes with higher baking temperatures, although presenting higher de-intercalation capacity, also show lower efficiency, indicating a larger degree of irreversible capacity loss. In addition, the anodes made using CMC:SBR present two distinguished peaks (below 300 mV) related to Li-ion intercalation staging into graphite.

Electrochemical impedance spectroscopy (EIS) studies

Electrochemical impedance spectroscopy (EIS—displayed in a Nyquist plot representation) studies of the MCMB composite anodes, utilizing the two types of binders at the two baking temperatures, are presented in Fig. 10, where the EIS measurements followed four cycles of CV. The Nyquist curves consist of two depressed semi-circles: the first semi-circle, at high frequencies, corresponds to the formed SEI, and the second semi-circle, at lower frequencies, is related to the charge transfer during lithiation/de-lithiation, followed by a low-frequency diffusion-controlled region. The impedance was fitted using an equivalent circuit (Fig. 10, inset), as shown in the model equation (Eq. 1).

This model for the equivalent circuit was chosen as it is common [47] and results in a good fit with our experimental data (see Table S1). The resistance R_s is ascribed to the electrolyte, and the contact resistance, R_{SEI}, is the resistance of the formed SEI film, and R_{CT} is the charge transfer resistance. Other elements are also present in the equivalent circuit, such as CPE (Constant phase element) and *W* (Warburg element). The CPE refers to the non-ideal polarizability of solid electrodes, which can be attributed to capacitance distribution originating from non-uniform surface, such as porous or fractal electrodes, or from non-uniform distribution of solution or interfacial capacitance (reaching different depths of pores, for example) [48]. The Warburg region at high frequencies refers to the limit where the system is controlled by the mass transfer of redox species to and from the interface region between the electrode and the electrolyte. Here, a skew from the typical 45° angle to lower angles can relate to the inhomogeneous distribution of the binder [49], and higher angles are a result of the capacitive character [50].

For the BSA-based electrodes baked at 2 different temperatures of 120 and 200 °C, the R_s values were found to be 0.9 and 0.8 Ω, respectively, while for the CMC:SBR based electrode, the values measured were 1.5 and 1.3 Ω (Table S1). These differences are in the range of the error limits of the measurements. Nevertheless, higher water content (at lower temperature electrode baking) could increase the surface resistance, as parasitic corrosion of the current collector may occur and, at the same time, electrolyte degradation may take place, as discussed earlier.

Charge transfer resistance appears to change drastically between the different binders and baking temperatures when

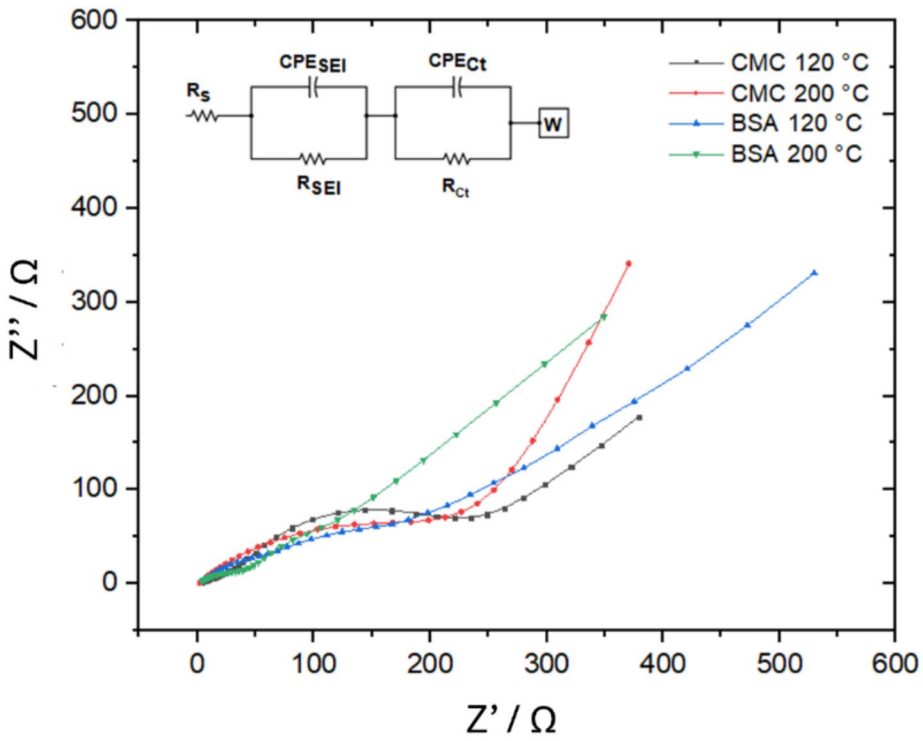

Fig. 10 Impedance measurements for the two different anode types, i.e., BSA- and CMC:SBR-based binders, processed at different baking temperatures after 4 CV runs. A schematic illustration for the equivalent circuit is shown as well

compared (see Table S1). This observation strengthens the speculation regarding rate change, which is related to the MCMB particles coverage by the baked binder. Hence, the trend of reduced charge transfer resistance is more dominant for BSA-based electrode (going down from 212 to ~ 41 Ω, compared with the reduction measured for the CMC:SBR-based electrod, showing a reduction from ~ 156 to ~ 98 Ω), as the network to surface contact was affected by the temperature more drastically, leading to major coverage modification (shrinking) of the binder.

Table S1 presents also a comparison of R_{SEI} for the four different anodes. R_{SEI} of the BSA-based anode, baked at 120 °C, is the largest, compared to the other anodes (~ 220 Ω). Water content embedded in the electrode can be directly correlated to the stability and the composition of the established SEI. A higher water content should lead to an increase in the portion of denser and passivating components, such as LiF, resulting in higher resistance. While referring to the structure of the binders, it is expected that BSA will retain a higher level of water compared to CMC:SBR; thus, the resistance is expected to be higher, and this tendency is clearly demonstrated in the lower baking temperature. However, baking at a higher temperature leads to water elimination from the electrode, as shown in the TGA results, and might explain the major reduction in the R_{SEI} values: for the BSA-based electrode, the value drops drastically from 220 to 34 Ω, and for the CMC:SBR-based electrodes, the value drops from 64 to 55 Ω.

Hence, baking the electrodes at high enough temperatures ensures water elimination from the MCMB-based electrode composition and may promote enhanced performance, as both R_{ct} and R_{SEI} are substantially reduced, and thus polarization losses are minimized.

Conclusions

This work addresses the impact of baking graphite anodes based on MCMB with water-borne binders for LIBs at a non-typical higher temperature. Crosslinked BSA, a unique configuration for a natural protein-based binder that is biodegradable and sustainably sourced from side-streams, and CMC:SBR, a more classic alternative to PVDF, were combined in a slurry with MCMB and baked at a temperature of 200 °C. The results show that baking at such high temperatures substantially improves the electrodes' performance, outperforming electrodes that experienced the usual drying approach at the temperature of 120 °C, stressing the importance of the baking process. This heat treatment procedure removes nearly all water from the composite anode electrodes, as evidenced by TGA and FTIR measurements, and induces beneficial structural changes within the anode. At the molecular level, residual water removal increases intra- and inter-molecular interactions in both binders, while seeming to maintain polymeric backbone integrity. At the morphological level, SEM studies reveal that the baking

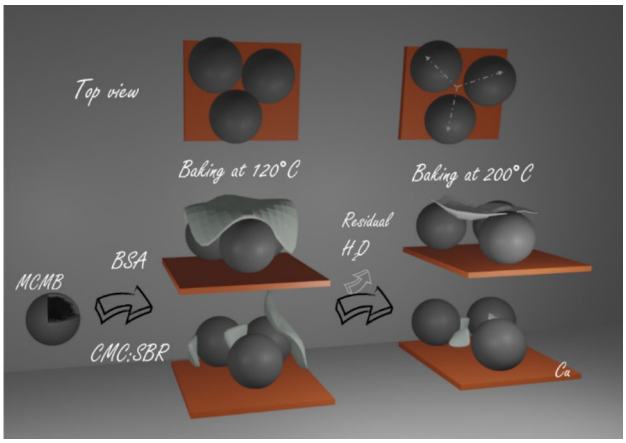

Fig. 11 Schematic summary of the results (effect of binder and baking temperature)

process at high temperatures mostly altered the distribution and covering of the MCMB active material particles by the binder, as shown schematically in Fig. 11.

In addition, increased temperature resulted in void formation and exposure of active surface area, which is likely well associated with the capacity increase. Electrochemical investigations, such as GCD, CV, and EIS, show improved reversible capacity, with crosslinked BSA-based anodes exhibiting exceptionally low irreversible capacity loss when compared to CMC:SBR anodes baked at 200 °C.

In summary, the main novelty presented in this work is the finding that elevating the baking temperature to 200 °C in water-based anode fabrication is not merely a drying step; it is a performance enabler and a crucial process while designing sustainable LIB anodes. A drying process of the anodes at 200 °C is leading to complete water evaporation from the composite electrode, hence eliminating parasitic side reactions, promoting beneficial microstructural evolution, and optimizing the binder-particles interface.

Supplementary Information The online version contains supplementary material available at https://doi.org/10.1007/s10008-025-06402-1.

Funding Open access funding provided by Technion - Israel Institute of Technology. This work was supported by the Israeli Ministry of Energy in the framework of Grant No. 221–11-047, by the Israel National Institute for Energy Storage (INIES), and by the Grand Technion Energy Program (GTEP).

References

1. Rao L, Jiao X, Yu CY, Schmidt A, O'Meara C, Seidt J, Sayre JR, Khalifa YM, Kim JH (2022) Multifunctional composite binder for thick high-voltage cathodes in lithium-ion batteries. ACS Appl Mater Interfaces. https://doi.org/10.1021/acsami.1c19554
2. Garsuch RR, Le D-B, Garsuch A, Li J, Wang S, Farooq A, Dahn JR (2008) Studies of lithium-exchanged nafion as an electrode binder for alloy negatives in lithium-ion batteries. J Electrochem Soc 155:A721. https://doi.org/10.1149/1.2956964
3. Ndour M, Bonnet J-P, Cavalaglio S, Lombard T, Przybylski C, Bonnet V (2019) CMC binding agent for silicon anodes in Li-ion batteries : the impact of the formulation. ECS Meet Abstr. https://doi.org/10.1149/MA2019-04/10/0471
4. Srivastava M, Anil AK, Zaghib K (2024) Binders for Li-ion battery technologies and beyond: a comprehensive review. Batteries 10:268. https://doi.org/10.3390/BATTERIES10080268
5. Rolandi AC, De Meatza I, Casado N, Forsyth M, Mecerreyes D, Pozo-Gonzalo C (2024). Unlocking sustainable power: advances in aqueous processing and water-soluble binders for NMC cathodes in high-voltage Li-ion batteries. https://doi.org/10.1039/d4su00098f
6. Peled E (1979) The electrochemical behavior of alkali and alkaline earth metals in nonaqueous battery systems—the solid electrolyte interphase model. J Electrochem Soc 126:2047–2051. https://doi.org/10.1149/1.2128859/XML
7. Aurbach D, Talyosef Y, Markovsky B, Markevich E, Zinigrad E, Asraf L, Gnanaraj JS, Kim HJ (2004) Design of electrolyte solutions for Li and Li-ion batteries: a review. Electrochim Acta 50:247–254. https://doi.org/10.1016/J.ELECTACTA.2004.01.090
8. Han JG, Kim K, Lee Y, Choi NS (2019) Scavenging materials to stabilize $LiPF_6$-containing carbonate-based electrolytes for Li-ion batteries. Adv Mater 31:1804822. https://doi.org/10.1002/ADMA.201804822
9. Sloop SE, Kerr JB, Kinoshita K (2003) The role of Li-ion battery electrolyte reactivity in performance decline and self-discharge. J Power Sources 119–121:330–337. https://doi.org/10.1016/S0378-7753(03)00149-6
10. Tan J, Matz J, Dong P, Shen J, Ye M, Tan J, Shen J, Ye M, Matz J, Dong P (2021) A growing appreciation for the role of LiF in the solid electrolyte interphase. Adv Energy Mater 11:2100046. https://doi.org/10.1002/AENM.202100046
11. Wang A, Kadam S, Li H, Shi S, Qi Y (2018) Review on modeling of the anode solid electrolyte interphase (SEI) for lithium-ion batteries. npj Comput Mater 2018 4:1–26. https://doi.org/10.1038/s41524-018-0064-0
12. Tasaki K, Harris SJ (2010) Computational study on the solubility of lithium salts formed on lithium ion battery negative electrode in organic solvents. J Phys Chem C Nanomater Interfaces 114:8076–8083. https://doi.org/10.1021/JP100013H
13. Hofmann K, Hegde AD, Liu-Theato X, Gordon R, Smith A, Willenbacher N (2024) Effect of mechanical properties on processing behavior and electrochemical performance of aqueous processed graphite anodes for lithium-ion batteries. J Power Sources 593:233996. https://doi.org/10.1016/J.JPOWSOUR.2023.233996

14. Françon HS, Gorur YC, Montanari C, Larsson PA, Wågberg L (2022) Toward li-ion graphite anodes with enhanced mechanical and electrochemical properties using binders from chemically modified cellulose fibers. ACS Appl Energy Mater 5:9333–9342. https://doi.org/10.1021/ACSAEM.2C00525
15. Jolley MJ, Pathan TS, Jenkins C, Loveridge MJ (2024) Investigating the effect of the degree of cross-linking in styrene butadiene rubber on the performance of graphite anodes for the use in lithium-ion batteries. J Appl Polym Sci 141:e55135. https://doi.org/10.1002/APP.55135
16. Nandi R, Agam Y, Amdursky N, Nandi R, Agam Y, Amdursky N (2021) A protein-based free-standing proton-conducting transparent elastomer for large-scale sensing applications. Adv Mater 33:2101208. https://doi.org/10.1002/ADMA.202101208
17. Soeda K, Yamagata M, Ishikawa M (2015) Alginic acid as a new aqueous slurry-based binder for cathode materials of LIB. ECS Trans 64:13–22. https://doi.org/10.1149/06418.0013ECST
18. Carrotta R, Manno M, Giordano FM, Longo A, Portale G, Martorana V, San Biagio PL (2009) Protein stability modulated by a conformational effector: effects of trifluoroethanol on bovine serum albumin. Phys Chem Chem Phys 11:4007–4018. https://doi.org/10.1039/B818687A
19. Dror Y, Ziv T, Makarov V, Wolf H, Admon A, Zussman E (2008) Nanofibers made of globular proteins. Biomacromolecules 9:2749–2754. https://doi.org/10.1021/BM8005243
20. Ruan X, He G, Li B, Xiao J, Dai Y (2014) Cleaner recovery of tetrafluoroethylene by coupling residue-recycled polyimide membrane unit to distillation. Sep Purif Technol 124:89–98. https://doi.org/10.1016/J.SEPPUR.2014.01.014
21. Yue M, Azam S, Zhang N, - al, Gómez-Pérez J, Kónya Z, Kukovecz Á, Wang H, Jiang F (2022) Experimental study on distillation and purification of reclaimed NMP. J Phys Conf Ser 2393:012022. https://doi.org/10.1088/1742-6596/2393/1/012022
22. Yang L, Chen Y, Wang J, Luo Y, Zhou P, Zhang X (2024) The simulation and optimization of the tetrafluoroethylene rectification process. Separations (2024) Vol 11. Page 37(11):37. https://doi.org/10.3390/SEPARATIONS11020037
23. Andersson LO (1969) Reduction and reoxidation of the disulfide bonds of bovine serum albumin. Arch Biochem Biophys 133:277–285. https://doi.org/10.1016/0003-9861(69)90455-X
24. Zhang Y, Murata S, Nomura M, Yamaguchi C (1999) Characterization of mesocarbon microbeads and their derivatives by IR, SEM and Raman spectroscopy. J Japan Petrol Inst 42:192–200. https://doi.org/10.1627/JPI1958.42.192
25. Cheng YL, Li TH, Li H, Jing DQ (2009) Preparation of mesocarbon microbeads and microstructure evolution. Proceedings of the International Symposium on the Physical and Failure Analysis of Integrated Circuits, IPFA 559–562. https://doi.org/10.1109/IPFA.2009.5232583
26. Alcañiz-Monge J, Cazorla-Amorós D, Linares-Solano A (2001) Characterisation of coal tar pitches by thermal analysis, infrared spectroscopy and solvent fractionation. Fuel 80:41–48. https://doi.org/10.1016/S0016-2361(00)00057-0
27. Hu L, Li Z, Wu Z, Lin L, Zhou S (2016) Catalytic hydrolysis of microcrystalline and rice straw-derived cellulose over a chlorine-doped magnetic carbonaceous solid acid. Ind Crops Prod 84:408–417. https://doi.org/10.1016/J.INDCROP.2016.02.039
28. Li HX, Zhang X, Wang Q, Yang D, Cao Q, Jin L (2020) Study on the hydrolysis of cellulose with the regenerable and recyclable multifunctional solid acid as a catalyst and its catalytic hydrolytic kinetics. Cellulose 27:285–300. https://doi.org/10.1007/S10570-019-02777-3
29. Penkov NV (2024) Water determines the intramolecular dynamics of proteins. An example of bovine serum albumin. Front Chem 12:1444448. https://doi.org/10.3389/FCHEM.2024.1444448
30. Molodenskiy D, Shirshin E, Tikhonova T, Gruzinov A, Peters G, Spinozzi F (2017) Thermally induced conformational changes and protein–protein interactions of bovine serum albumin in aqueous solution under different pH and ionic strengths as revealed by SAXS measurements. Phys Chem Chem Phys 19:17143–17155. https://doi.org/10.1039/C6CP08809K
31. Mücksch C, Urbassek HM (2011) Molecular dynamics simulation of free and forced BSA adsorption on a hydrophobic graphite surface. Langmuir 27:12938–12943. https://doi.org/10.1021/LA201972F
32. Usoltsev D, Sitnikova V, Kajava A, Uspenskaya M (2019) Systematic FTIR spectroscopy study of the secondary structure changes in human serum albumin under various denaturation conditions. Biomolecules (2019) Vol 9. Page 359(9):359. https://doi.org/10.3390/BIOM9080359
33. Lin VJC, Koenig JL (1976) Raman studies of bovine serum albumin. Biopolymers 15:203–218. https://doi.org/10.1002/BIP.1976.360150114
34. Park JH, Jackman JA, Ferhan AR, Ma GJ, Yoon BK, Cho NJ (2018) Temperature-induced denaturation of BSA protein molecules for improved surface passivation coatings. ACS Appl Mater Interfaces 10:32047–32057. https://doi.org/10.1021/ACSAMI.8B13749
35. Smith MB, March J (2006) March's advanced organic chemistry. March's Advanced Organic Chemistry. https://doi.org/10.1002/0470084960
36. Militello V, Casarino C, Emanuele A, Giostra A, Pullara F, Leone M (2004) Aggregation kinetics of bovine serum albumin studied by FTIR spectroscopy and light scattering. Biophys Chem 107:175–187. https://doi.org/10.1016/J.BPC.2003.09.004
37. Conformation of bovine serum albumin as a function of hydration monitored by infrared spectroscopy | The Infrared and Raman Discussion Group. https://www.irdg.org/ijvs/ijvs-volume-6-edition-1/conformation-of-bovine-serum-albumin-as-a-function-of-hydration-monitored-by-infrared-spectroscopy. Accessed 4 Jun 2025
38. Lim S, Kim S, Ahn KH, Lee SJ (2015) The effect of binders on the rheological properties and the microstructure formation of lithium-ion battery anode slurries. J Power Sources 299:221–230. https://doi.org/10.1016/J.JPOWSOUR.2015.09.009
39. Navarra MA, Dal Bosco C, Moreno JS, Vitucci FM, Paolone A, Panero S (2015) Synthesis and characterization of cellulose-based hydrogels to be used as gel electrolytes. Membranes 5:810–823. https://doi.org/10.3390/MEMBRANES5040810
40. Tufan MZ, Kaplan AN, Özel C (2025) Enhancing concrete microstructure with carboxymethyl cellulose (CMC) and microcrystalline cellulose (MCC): a comprehensive characterization using FTIR, TGA, and XRD. J Build Eng 106:112611. https://doi.org/10.1016/J.JOBE.2025.112611
41. Ma Y, Ma J, Cui G (2019) Small things make big deal: powerful binders of lithium batteries and post-lithium batteries. Energy Storage Mater 20:146–175. https://doi.org/10.1016/J.ENSM.2018.11.013
42. Boruvkova K, Wiener J, Kukreja S (2012) Thermal self cross-linking of carboxymethylcellulose. ACC Journal (Academic Coordination Centre at the Euroregion Neisse), Issue A:6–13. https://acc-ern.tul.cz/archiv/PDF/ACC_2012_1_01.pdf
43. Hagiwara H, Suszynski WJ, Francis LF (2014) A raman spectroscopic method to find binder distribution in electrodes during

drying. J Coat Technol Res 11:11–17. https://doi.org/10.1007/S11998-013-9509-Z
44. Kumberg J, Bauer W, Schmatz J, Diehm R, Tönsmann M, Müller M, Ly K, Scharfer P, Schabel W (2021) Reduced drying time of anodes for lithium-ion batteries through simultaneous multilayer coating. Energy Technol. https://doi.org/10.1002/ENTE.202100367
45. Guo Z, Zhu J, Feng J, Du S (2015) Direct in situ observation and explanation of lithium dendrite of commercial graphite electrodes. RSC Adv 5:69514–69521. https://doi.org/10.1039/C5RA13289D
46. Zhao X, Chen Y, Sun H, Yuan T, Gong Y, Liu X, Chen T (2023) Impact of surface structure on SEI for carbon materials in alkali ion batteries: a review. Batteries (Basel). https://doi.org/10.3390/batteries9040226
47. Morasch R, Gasteiger HA, Suthar B (2024) Li-ion battery material impedance analysis II: graphite and solid electrolyte interphase kinetics. J Electrochem Soc 171:050548. https://doi.org/10.1149/1945-7111/AD48C0
48. Lasia A (2022) The origin of the constant phase element. J Phys Chem Lett 13:580–589. https://doi.org/10.1021/ACS.JPCLETT.1C03782
49. Landesfeind J, Eldiven A, Gasteiger HA (2018) Influence of the binder on lithium ion battery electrode tortuosity and performance. J Electrochem Soc 165:A1122–A1128. https://doi.org/10.1149/2.0971805JES
50. Laschuk NO, Easton EB, Zenkina OV (2021) Reducing the resistance for the use of electrochemical impedance spectroscopy analysis in materials chemistry. RSC Adv 11:27925–27936. https://doi.org/10.1039/D1RA03785D